

## A Family of Manganese Rods: Syntheses, Structures, and Magnetic Properties

Gopalan Rajaraman,<sup>†</sup> Muralee Murugesu,<sup>‡</sup> E. Carolina Sañudo,<sup>‡</sup> Monica Soler,<sup>‡</sup>  
Wolfgang Wernsdorfer,<sup>||</sup> Madeleine Helliwell,<sup>†</sup> Chris Muryn,<sup>†</sup> Jim Raftery,<sup>†</sup>  
Simon J. Teat,<sup>§</sup> George Christou,<sup>‡</sup> and Euan K. Brechin<sup>\*,†,¶</sup>

Contribution from the Department of Chemistry, The University of Manchester, Oxford Road, Manchester, M13 9PL, United Kingdom, Department of Chemistry, University of Florida, Gainesville, Florida 32611-7200, CCLRC Daresbury Laboratory, Daresbury, Warrington, Cheshire, WA4 4AD, United Kingdom, Laboratoire Louis Néel-CNRS, 38042 Grenoble, Cedex 9, France, and School of Chemistry, The University of Edinburgh, West Mains Road, Edinburgh, EH9 3JJ, United Kingdom

Received May 13, 2004; E-mail: ebrechin@staffmail.ed.ac.uk

**Abstract:** The reaction of the mixed-valent metal triangles  $[\text{Mn}_3\text{O}(\text{O}_2\text{CR})_6(\text{py})_3]$  ( $\text{R} = \text{CH}_3, \text{Ph}, \text{C}(\text{CH}_3)_3$ ) with the tripodal ligands  $\text{H}_3\text{thme}$  (1,1,1-tris(hydroxymethyl)ethane) and  $\text{H}_3\text{tmp}$  (1,1,1-tris(hydroxymethyl)propane) in MeCN, produces a family of manganese rodlike complexes whose structures are all derived from a series of edge-sharing triangles. Variable temperature direct current (dc) magnetic susceptibility data were collected for all complexes in the 1.8–300 K temperature range in fields up to 7.0 T. Complex **1**,  $[\text{Mn}_{12}\text{O}_4(\text{OH})_2(\text{PhCOO})_{12}(\text{thme})_4(\text{py})_2]$ , has an  $S = 7$  ground state with the parameters  $g = 1.98$  and  $D = -0.13$  K. Complex **2**,  $[\text{Mn}_8\text{O}_4((\text{CH}_3)_3\text{CCO}_2)_{10}(\text{thme})_2(\text{py})_2]$  has a ground state of  $S = 6$ , with  $g = 1.81$  and  $D = -0.36$  K. Complex **3**,  $[\text{Mn}_7\text{O}_2(\text{PhCO}_2)_9(\text{thme})_2(\text{py})_3]$ , has a spin ground states of  $S = 7$  with the parameters  $g = 1.78$  and  $D = -0.20$  K. The best fit for complex **4**,  $[\text{Mn}_6((\text{CH}_3)_3\text{CCO}_2)_8(\text{tmp})_2(\text{py})_2]$ , gave a spin ground state of  $S = 3$  with the parameters  $g = 1.73$  and  $D = -0.75$  K, but was of poorer quality than that normally obtained. The presence of multiple  $\text{Mn}^{2+}$  ions in the structure of **4** leads to the presence of low-lying excited states with energy levels very close to the ground state, and in the case of complex **5**,  $[\text{Mn}_6(\text{CH}_3\text{CO}_2)_6(\text{thme})_2(\text{H}_2\text{tea})_2]$ , no satisfactory fit of the data was obtained. DFT calculations on **4** and **5** indicate complexes with spin ground states of  $S = 4$  and  $S = 0$  respectively, despite their topological similarities. Single-crystal hysteresis loop and relaxation measurements show complex **1** to be a SMM.

### Introduction

The synthesis of polymetallic clusters of manganese has been stimulated by two main fields. The first is biological in origin, as Mn is prominent in the active sites of many metallo-biomolecules,<sup>1</sup> and the second is the discovery of molecules that can function as nanoscale magnets below a critical temperature.<sup>2</sup> Such Single-Molecule Magnets (SMMs) not only display magnetization hysteresis, but also quantum tunneling of magnetization (QTM)<sup>3</sup> and quantum phase interference (QPI),<sup>4</sup> and as such they are promising new materials for data storage and quantum computing. Mn clusters often display abnormally large spin ground states (with respect to other 3d

transition metal clusters) and this, coupled with a large zero-field splitting parameter ( $D$ ) (derived from the presence of Jahn–Teller distorted  $\text{Mn}^{3+}$  ions) gives rise to the superparamagnetic-like property of a barrier to magnetization relaxation,<sup>5</sup> which can be observed as out-of-phase signals in ac susceptibility measurements<sup>6</sup> or hysteresis loops in magnetization vs. dc field studies.<sup>7</sup>

One important goal in this area of chemistry is not just to make new examples of high spin molecules and SMMs, but also to build up families of related compounds so that structure–property relations can be investigated. Toward this end, two successful but opposing strategies have been employed. The first is the use of rigid bridging ligands that impose the geometry

<sup>†</sup> Department of Chemistry, The University of Manchester.

<sup>‡</sup> Department of Chemistry, University of Florida.

<sup>§</sup> CCLRC Daresbury Laboratory.

<sup>||</sup> Laboratoire Louis Néel-CNRS.

<sup>¶</sup> School of Chemistry, The University of Edinburgh.

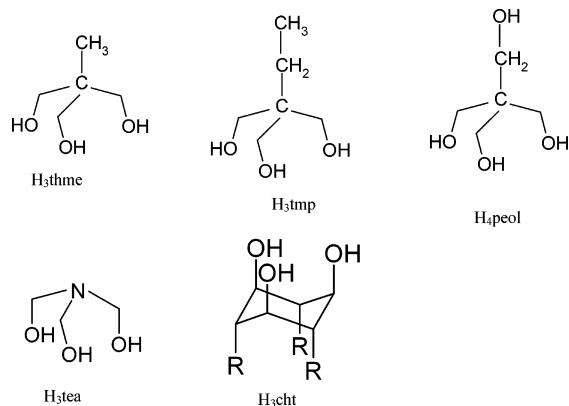
- (1) (a) *Manganese Redox Enzymes*; Pecoraro, V. L., Ed.; VCH Publishers: New York, 1992. (b) Christou, G. *Acc. Chem. Res.* **1989**, *22*, 328–335.
- (2) (a) Sessoli, R.; Tsai, H.-L.; Schake, A. R.; Wang, S.; Vincent, J. B.; Folting, K.; Gatteschi, D.; Christou, G.; Hendrickson, D. N. *J. Am. Chem. Soc.* **1993**, *115*, 1804–1816. (b) Sessoli, R.; Gatteschi, D.; Caneschi, A.; Novak, M. A. *Nature* **1993**, *365*, 141–143.
- (3) Friedman, J. R.; Sarachik, M. P.; Tejada, J.; Ziolo, R. *Phys. Rev. Lett.* **1996**, *76*, 3830–3833.
- (4) Wernsdorfer, W.; Sessoli, R. *Science* **1999**, *284*, 133–135.

- (5) Sessoli, R.; Gatteschi, D.; Hendrickson, D. N.; Christou, G. *MRS Bull.* **2000**, *25*, 66–71.

- (6) See for example Boskovic, C.; Brechin, E. K.; Streib, W. E.; Folting, K.; Bollinger, J. C.; Hendrickson, D. N.; Christou, G. *J. Am. Chem. Soc.* **2002**, *124*, 3725–3736.

- (7) See for example: (a) Brechin, E. K.; Soler, M.; Christou, G.; Davidson, J.; Hendrickson, D. N.; Parsons, S.; Wernsdorfer, W. *Polyhedron* **2003**, *22*, 1771–1775. (b) Soler, M.; Wernsdorfer, W.; Folting, K.; Pink, M.; Christou, G. *J. Am. Chem. Soc.* **2004**, *126*, 2156–2165. (c) Jones, L. F.; Brechin, E. K.; Collison, D.; Harrison, A.; Teat, S. J.; Wernsdorfer, W. *Chem. Commun.* **2002**, 2974–2975. (d) Tasiopoulos, A. J.; Vinslava, A.; Wernsdorfer, W.; Abboud, K. A.; Christou, G. *Angew. Chem., Int. Ed.* **2004**, *43*, 2117–2121.

**Scheme 1.** Tripodal Ligands 1,1,1-Tris(hydroxymethyl)ethane (H<sub>3</sub>thme); 1,1,1-Tris(hydroxymethyl)propane (H<sub>3</sub>tmp); Pentaerythritol (H<sub>4</sub>peol); Triethanolamine (H<sub>3</sub>tea); 1,3,5-Cyclohexanetriol (H<sub>3</sub>cht)



on the resultant cluster,<sup>8</sup> and the second is the use of flexible ligands that impose little or no geometry.<sup>9</sup>

Tripodal ligands such as 1,1,1-tris(hydroxymethyl)ethane (H<sub>3</sub>thme, Scheme 1) and 1,1,1-tris(hydroxymethyl)propane (H<sub>3</sub>tmp) have previously been used in the synthesis of oxovanadium and oxo-molybdenum clusters,<sup>10</sup> but until recently, rarely in the synthesis of paramagnetic 3d transition metal clusters. In polyoxometalate chemistry, the disposition of the three alkoxide arms of the tri-anion directs the formation of triangular M<sub>3</sub> units, where each arm of the ligand bridges one edge of the triangle. These units then combine to form complexes whose structures are commonly based on octahedra. For clusters of 3d metals however, these units can combine in more diverse ways and produce more elaborate products when the tripodal ligands are used in combination with other flexible ligands, such as carboxylates and/or by changes in the nature of the tripod itself: for example, by using a ligand containing one or two amine arms, rather than three alkoxides arms. If paramagnetic clusters can be designed in such a way as to contain many triangular building blocks or units, then the products have a greater chance of displaying high or at least nonzero spin ground states, due to the presence of the large number of competing antiferromagnetic exchange interactions that would be present.

We have been investigating the use of tripodal ligands in the synthesis of polynuclear clusters of 3d transition metals including Mn,<sup>11</sup> Fe,<sup>12</sup> Cr,<sup>13</sup> Co,<sup>14</sup> and Ni,<sup>15</sup> and here report the continuation of this work with the syntheses and magnetic

properties of a family of high-spin Mn clusters built using tripodal ligands, where the directed M<sub>3</sub> units edge-share to form structures based on rods. We also demonstrate the use of DFT calculations as a tool in understanding the nature of exchange interactions and ground-state spin structures in polynuclear transition metal clusters. In particular, we show that theoretical calculations<sup>16</sup> can be used to explain why compounds with similar metallic cores can display markedly different magnetic properties.

## Experimental Section

**[Mn<sub>12</sub>O<sub>4</sub>(OH)<sub>2</sub>(PhCOO)<sub>12</sub>(thme)<sub>4</sub>(py)<sub>2</sub>] 1.** [Mn<sub>3</sub>O(PhCO<sub>2</sub>)<sub>6</sub>(py)<sub>3</sub>] (0.5 g) and H<sub>3</sub>thme (0.08 g) were added to MeCN (20 mL) and the solution stirred for 30 min. After this period the solution was filtered and Et<sub>2</sub>O diffused into the solution. Crystals of **1** grew in approximately 20% yield after 1 week. Elemental analysis, calcd (%) for C<sub>114</sub>H<sub>108</sub>N<sub>2</sub>O<sub>42</sub>-Mn<sub>12</sub> (**1**): C 48.25, H 3.84, N 0.99, Mn 23.23; found: C 48.43, H 3.99, N 1.14, Mn 23.18.

**Crystal Data for 1·2.25 Et<sub>2</sub>O:** C<sub>123</sub>H<sub>130.5</sub>Mn<sub>12</sub>N<sub>2</sub>O<sub>44.5</sub>, monoclinic, *P*2<sub>1</sub>/*c*, *a* = 18.4232(10), *b* = 28.2986(15), *c* = 26.5871(14) Å, α = 90°, β = 90.085(2)°, γ = 90°, *V* = 13 861.2(13) Å<sup>3</sup>, *M* = 3004.07, *Z* = 4, *T* = 150(2) K, μ = 1.132 mm<sup>-1</sup>, Synchrotron radiation (CCLRC Daresbury Laboratory, Station 9.8,<sup>17</sup> λ = 0.6867 Å), 61081 reflections collected, 19860 unique, (*R*<sub>int</sub> = 0.0492) 2θ<sub>max</sub> = 44.83°, *R*1 = 0.0732 [13320 data with *I* > 2σ(*F*)], *wR*2 = 0.2086 for 1815 parameters. CCDC 204 631.

**[Mn<sub>8</sub>O<sub>4</sub>((CH<sub>3</sub>)<sub>3</sub>CCO<sub>2</sub>)<sub>10</sub>(thme)<sub>2</sub>(py)<sub>2</sub>] 2.** [Mn<sub>3</sub>O((CH<sub>3</sub>)<sub>3</sub>CCO<sub>2</sub>)<sub>6</sub>(py)<sub>3</sub>] (0.5 g) and H<sub>3</sub>thme (0.08 g) were added to MeCN (20 mL) and the solution stirred for 30 min. After this period the solution was filtered and allowed to stand. Crystals of **2** grew in approximately 20% yield after 1 week. Elemental analysis, calcd (%) for C<sub>72</sub>H<sub>121</sub>N<sub>3</sub>O<sub>30</sub>Mn<sub>8</sub> (**2**·1 MeCN): C 44.39, H 6.26, N 2.16, Mn 22.56; found: C 44.46, H 6.40, N 2.25, Mn 22.62.

**Crystal Data for 2·4MeCN·3H<sub>2</sub>O:** C<sub>78</sub>H<sub>133</sub>Mn<sub>8</sub>N<sub>6</sub>O<sub>33</sub>, monoclinic, *P*2<sub>1</sub>/*c*, *a* = 17.332(2), *b* = 12.552(2), *c* = 25.289(3) Å, α = 90°, β = 108.864(7)°, γ = 90°, *V* = 5203.1(12) Å<sup>3</sup>, *M* = 2122.42, *Z* = 2, *T* = 150(2) K, μ = 1.012 mm<sup>-1</sup>, Synchrotron radiation (CCLRC Daresbury Laboratory, Station 9.8,<sup>17</sup> λ = 0.6845 Å), 7735 reflections collected, 5119 unique, (*R*<sub>int</sub> = 0.0359) 2θ<sub>max</sub> = 40°, *R*1 = 0.0572 [3639 data with *I* > 2σ(*F*)], *wR*2 = 0.1574 for 533 parameters. CCDC 204632.

**[Mn<sub>7</sub>O<sub>2</sub>(PhCO<sub>2</sub>)<sub>9</sub>(thme)<sub>2</sub>(py)<sub>3</sub>] 3.** [Mn<sub>3</sub>O(PhCO<sub>2</sub>)<sub>6</sub>(py)<sub>3</sub>] (0.5 g) and H<sub>3</sub>thme (0.08 g) were added to MeCN (20 mL) and pyridine (5 mL) and the solution stirred for 30 min. After this period, the solution was filtered and allowed to stand. Crystals of **3** grew in approximately 20% yield after 1 week. Elemental analysis, calcd (%) for C<sub>93</sub>H<sub>83</sub>N<sub>4</sub>O<sub>26</sub>Mn<sub>7</sub> (**3**·1 py): C 54.30, H 4.07, N 2.72, Mn, 18.69; found: C 54.48, H 4.12, N 2.80, Mn 18.90.

**Crystal Data for 3·1.5py·1.5MeCN:** C<sub>98.5</sub>H<sub>90</sub>Mn<sub>7</sub>N<sub>6</sub>O<sub>26</sub>, monoclinic, *P*2<sub>1</sub>/*c*, *a* = 22.87(10), *b* = 24.02(8), *c* = 19.10(8) Å, α = 90°, β = 111.0(2)°, γ = 90°, *V* = 9797(69) Å<sup>3</sup>, *M* = 2158.34, *Z* = 4, *T* = 100(2) K, μ = 0.951 mm<sup>-1</sup>, 49 589 reflections collected, 49 593 unique, (*R*<sub>int</sub> = 0.000) 2θ<sub>max</sub> = 50.06°, *R*1 = 0.0668 [39 983 data with *I* > 2σ(*F*)], *wR*2 = 0.1983 for 1226 parameters. CCDC 238285.

**[Mn<sub>6</sub>((CH<sub>3</sub>)<sub>3</sub>CCO<sub>2</sub>)<sub>8</sub>(tmp)<sub>2</sub>(py)<sub>2</sub>] 4.** [Mn<sub>3</sub>O((CH<sub>3</sub>)<sub>3</sub>CCO<sub>2</sub>)<sub>6</sub>(py)<sub>3</sub>] (0.5 g) and H<sub>3</sub>tmp (0.08 g) were added to MeCN (20 mL) and the solution stirred for 30 min. After this period the solution was filtered and allowed

- (8) (a) Marvaud, V.; Decroix, C.; Scuiller, A.; Guyard-Duhayon, C.; Vaissermann, J.; Gonnet, F.; Verdaguer, M. *Chem. Eur. J.* **2003**, *9*, 1677–1691. (b) Scuiller, A.; Mallah, T.; Verdaguer, M.; Nivorozhkin, A.; Thiolence, J. L.; Veillet, P. *New J. Chem.* **1996**, *20*, 1–3. (c) Sokol, J. J.; Hee, A. G.; Long, J. R. *J. Am. Chem. Soc.* **2002**, *124*, 7656–7657. (d) Choi, H. J.; Sokol, J. J.; Long, J. R. *Inorg. Chem.* **2004**, *43*, 1606–1608. (e) Berlinguette, C. P.; Vaughn, D.; Canada-Vilalta, C.; Galan-Mascaros, J. R.; Dunbar, K. M. *Angew. Chem., Int. Ed.* **2003**, *42*, 1523–1526.
- (9) See for example: Brechin, E. K.; Boskovic, C.; Wernsdorfer, W.; Yoo, J.; Yamaguchi, A.; Sanudo, C.; Concolino, T.; Rheingold, A. L.; Ishimoto, H.; Hendrickson, D. N.; Christou, G. *J. Am. Chem. Soc.* **2002**, *124*, 9710–9711.
- (10) (a) Khan, M. I.; Zubieta, J. *Prog. Inorg. Chem.* **1995**, *43*, 1–149. (b) Cavaluzzo, M.; Chen, Q.; Zubieta, J. *J. Chem. Soc., Chem. Commun.* **1993**, 131–132. (c) Finn, R. C.; Zubieta, J. *J. Cluster Science* **2000**, *11*, 461–482. (d) Saalfrank, R. W.; Bernt, I.; Uller, E.; Hampel, F. *Angew. Chem., Int. Ed. Engl.* **1997**, *36*, 2482–2485.
- (11) Brechin, E. K.; Soler, M.; Davidson, J.; Hendrickson, D. N.; Parsons, S.; Christou, G. *Chem. Commun.* **2002**, 2252–2253.
- (12) Jones, L. F.; Batsanov, A.; Brechin, E. K.; Collison, D.; Helliwell, M.; Mallah, T.; McInnes, E. J. L.; Piligkos, S. *Angew. Chem., Int. Ed.* **2002**, *41*, 4318–4321.

- (13) Talbot-Eeckelaers, C.; Rajaraman, G. C.; Aromí, G.; Brechin, E. K. *Dalton Trans.*, submitted.
- (14) Talbot-Eeckelaers, C.; Moragues-Canovas, M.; Brechin, E. K.; Mallah, T. *Chem. Commun.*, submitted.
- (15) Moragues-Canovas, M.; Helliwell, M.; Ricard, L.; Rivière, É.; Wernsdorfer, W.; Brechin, E. K.; Mallah, T. *Eur. J. Inorg. Chem.* **2004**, 2219–2212.
- (16) Ruiz, E.; Fortea, A. R.; Cano, J.; Alvarez, S.; Alemany, P. *J. Comput. Chem.* **2003**, *24*, 982–989.
- (17) Cemik, R. J.; Clegg, W.; Catlow, C. R. A.; Bushnell-Wye, G.; Flaherty, J. V.; Greaves, G. N.; Burrows, I.; Taylor, D. J.; Teat, S. J.; Hamichi, M. J. *Synchrotron. Radiat.* **1997**, *4*, 279–286.

to stand. Crystals of **4** grew in approximately 20% yield after 1 week. Elemental analysis, calcd (%) for  $C_{62}H_{104}N_2O_{22}Mn_6$  (**4**): C 47.76, H 6.72, N 1.80, Mn 21.14; found: C 47.91, H 6.75, N 1.88, Mn 21.25.

**Crystal Data for 4·1MeCN·1H<sub>2</sub>O:**  $C_{64}H_{104}Mn_6N_3O_{24}$ , triclinic, *P*-1, *a* = 11.3948(16), *b* = 15.726(2), *c* = 24.969(4) Å,  $\alpha$  = 82.751(2)°,  $\beta$  = 79.881(2)°,  $\gamma$  = 70.683(2)°, *V* = 4145.5(10) Å<sup>3</sup>, *M* = 1629.14, *Z* = 2, *T* = 100(2) K,  $\mu$  = 0.953 mm<sup>-1</sup>,  $\lambda$  = 0.710 73 Å, 16 644 reflections collected, 10 839 unique, (*R*<sub>int</sub> = 0.0587)  $2\theta_{max}$  = 52.74°, *R*1 = 0.0761 [10 839 data with *I* > 2σ(*F*)], *wR*2 = 0.1100 for 800 parameters. CCDC 238286.

**[Mn<sub>6</sub>(CH<sub>3</sub>CO<sub>2</sub>)<sub>6</sub>(thme)<sub>2</sub>(H<sub>2</sub>tea)<sub>2</sub>] 5.** [Mn<sub>3</sub>O(CH<sub>3</sub>)<sub>3</sub>CO<sub>2</sub>)<sub>6</sub>(py)<sub>3</sub>] (0.5 g), H<sub>3</sub>thme (0.08 g) and H<sub>3</sub>tea (0.05 g) were added to MeCN (20 mL) and the solution stirred for 30 min. After this period, the solution was filtered and allowed to stand. Crystals of **5** grew in approximately 20% yield after 1 week. Elemental analysis, calcd (%) for  $C_{36}H_{67}N_3O_{24}Mn_6$  (**5**·1 MeCN): C 34.44, H 5.37, N 3.35, Mn 26.25; found: C 34.62, H 5.75, N 3.56, Mn 26.25.

**Crystal Data for 5·2.4 MeCN:**  $C_{38.80}H_{67.20}Mn_6N_{4.40}O_{24}$ , monoclinic, *C*2/*c*, *a* = 27.271(7), *b* = 11.354(2), *c* = 21.163(3) Å,  $\alpha$  = 90°,  $\beta$  = 122.19(4)°,  $\gamma$  = 90°, *V* = 5546 (2) Å<sup>3</sup>, *M* = 1309.1, *Z* = 4, *T* = 100(2) K,  $\mu$  = 1.406 mm<sup>-1</sup>, 22 278 reflections collected, 6866 unique, (*R*<sub>int</sub> = 0.0359)  $2\theta_{max}$  = 40°, *R*1 = 0.0718 [6866 data with *I* > 2σ(*F*)], *wR*2 = 0.1305 for 346 parameters. CCDC 238287.

Data collection, structure solution and refinement used programs SMART,<sup>18</sup> SAINT<sup>19</sup> and SHELXL.<sup>20</sup>

**Magnetic Measurements.** Variable-temperature, solid-state direct current (dc) magnetic susceptibility data down to 1.80 K were collected on a Quantum Design MPMS-XL SQUID magnetometer equipped with a 7 T dc magnet at the University of Florida. Diamagnetic corrections were applied to the observed paramagnetic susceptibilities using Pascal's constants. The dc measurements below 1.80 K were performed on single crystals using an array of micro-SQUIDS.<sup>21</sup>

## Results and Discussion

**Syntheses.** When the tripodal ligands H<sub>3</sub>thme and H<sub>3</sub>tmp are used in conjunction with Mn carboxylate triangles elaborate arrays of M<sub>3</sub> units are obtained. The complexes that result have structures that are all closely related, but whose subtle differences depend on (i) the identity of the tripod, (ii) the identity of the carboxylate, and (iii) the presence or absence of base. Here, we describe the synthesis of structurally related [Mn<sub>12</sub>], [Mn<sub>8</sub>], [Mn<sub>7</sub>], and [Mn<sub>6</sub>] rodlike complexes all built from edge-sharing M<sub>3</sub> triangular units. When the trinuclear complex [Mn<sub>3</sub>O(PhCO<sub>2</sub>)<sub>6</sub>(py)<sub>3</sub>] is reacted with H<sub>3</sub>thme in MeCN the product that results is a dodecanuclear Mn complex (**1**) consisting of 10 edge-sharing M<sub>3</sub> units. When the identical reaction is performed but replacing benzoate with pivalate, an octanuclear Mn complex (**2**) consisting of six edge-sharing triangles is formed. Complex **2** crystallizes more quickly than complex **1** and so the differences in the observed structures may simply be due to solubility. When the initial reaction between the [Mn<sub>3</sub>O(PhCO<sub>2</sub>)<sub>6</sub>(py)<sub>3</sub>] triangle and H<sub>3</sub>thme in MeCN is repeated, but in the presence of pyridine, a heptanuclear Mn cluster (**3**) consisting of five edge-sharing triangles is formed. This perhaps suggests that the addition of base, and therefore the faster deprotonation of the tripodal ligand, results in the formation of a similar, but smaller, Mn rod. However, when the tripodal ligand H<sub>3</sub>tmp is reacted with the pivalate triangle [Mn<sub>3</sub>O((CH<sub>3</sub>)<sub>3</sub>CCO<sub>2</sub>)<sub>6</sub>(py)<sub>3</sub>] in MeCN, a hexanuclear Mn rod

(**4**) consisting of four edge-sharing triangles is formed. This is essentially the same reaction which produces the octanuclear complex, **2**, but where the tripodal ligand has changed from H<sub>3</sub>thme to H<sub>3</sub>tmp. Complex **4** forms quickly in high yield, possibly because the combination of both the bulky pivalate ions and larger tmp<sup>3-</sup> ions promote stronger intermolecular interactions which aids the crystallization process. The reaction between the [Mn<sub>3</sub>O(CH<sub>3</sub>CO<sub>2</sub>)<sub>6</sub>(py)<sub>3</sub>] triangle and H<sub>3</sub>thme in the presence of a capping ligand (H<sub>3</sub>tea) produces a similar hexanuclear rod (**5**) to complex **4**, where the triethanolamine ligands simply replace the terminal pyridine molecules and peripheral pivalate ligands. Complex **5** forms quickly in high yield, suggesting that the use of a capping ligand quickly arrests the growth of the rodlike cluster, forming the smallest possible species.

However, all of the above complexes demonstrate different levels of oxidation, even though they are all prepared from [Mn<sup>III</sup>Mn<sup>II</sup>] triangles: complex **1** has a [Mn<sup>III</sup><sub>10</sub>Mn<sup>II</sup><sub>2</sub>] core; complex **2** has a [Mn<sup>III</sup><sub>8</sub>] core; complex **3** has a [Mn<sup>III</sup><sub>5</sub>Mn<sup>II</sup><sub>2</sub>] core, and complexes **4** and **5** both have [Mn<sup>III</sup><sub>2</sub>Mn<sup>II</sup><sub>4</sub>] cores. This is consistent with the multiple aggregation of mixed-valent [Mn<sub>3</sub>] units directed by tripodal ligands, and their subsequent crystallization depending on their solubilities, as governed by differences in carboxylates and the presence or absence of intermolecular interactions. However, as is the case with almost all Mn cluster chemistry, these products are unlikely to be the only species present. The tripodal ligands are added in their fully protonated state, H<sub>3</sub>tripod, and yet appear in the products in their fully deprotonated, tripod<sup>3-</sup>, form even if no base is added. This means that the formation of complexes **1**–**5** must also involve the protonation/deprotonation, structural rearrangement and redox chemistry of other species present in solution.

**Crystal Structures.** The structure of complex **1**, [Mn<sub>12</sub>O<sub>4</sub>(OH)<sub>2</sub>(PhCO<sub>2</sub>)<sub>12</sub>(thme)<sub>4</sub>(py)<sub>2</sub>], is shown in Figure 1 and selected bond lengths and angles in Table 1. The core of **1** consists of a [Mn<sup>III</sup><sub>10</sub>Mn<sup>II</sup><sub>2</sub>O<sub>4</sub>(OH)<sub>2</sub>]<sup>24+</sup> rod- or ladder-like unit where Mn1 and Mn12 are, respectively, above and below the plane of the central ten Mn ions. The [Mn<sup>III</sup><sub>10</sub>Mn<sup>II</sup><sub>2</sub>O<sub>4</sub>(OH)<sub>2</sub>]<sup>24+</sup> core is trapped-valence, with Mn3 and Mn10 being the Mn<sup>2+</sup> ions, and can be described as consisting of 10 edge-sharing [Mn<sub>3</sub>O] triangles or five edge-sharing [Mn<sub>4</sub>O<sub>2</sub>] butterfly units. All twelve Mn ions are in distorted octahedral geometries with the ten Mn<sup>3+</sup> ions displaying the expected Jahn–Teller elongations, although these are not co-parallel. The four thme<sup>3-</sup> ligands are fully deprotonated, sitting directly above and below the [Mn<sup>III</sup><sub>10</sub>Mn<sup>II</sup><sub>2</sub>O<sub>4</sub>(OH)<sub>2</sub>]<sup>24+</sup> plane, and are of two types: two use two of their arms in a  $\mu_2$ -fashion with the third arm acting as a  $\mu_3$ -bridge; the reverse situation applies for the other two thme<sup>3-</sup> ligands which have two  $\mu_3$ -arms and one  $\mu_2$ -arm. The PhCO<sub>2</sub><sup>-</sup> ligands bridge in their usual syn, syn,  $\mu$ -manner with the remaining coordination sites occupied by two pyridines. Two of the four O<sup>2-</sup> ions (O1, O34) are found in the peripheral [Mn<sub>3</sub>O] units, while two (O18, O22) are found in the innermost [Mn<sub>3</sub>O] units. The two OH<sup>-</sup> ions (O19, O23) are  $\mu_2$ -bridging, again found in the center of the rod, each bridging one edge of the innermost [Mn<sub>3</sub>O] units. In the crystal, the [Mn<sub>12</sub>] molecules pack in two directions with each cluster effectively 'insulated' from its neighbor by the presence of two and a quarter molecules of diethyl ether. However, there remains some close contact between benzoate ions on adjacent clusters (C...C, ~4.0–4.3

(18) SMART, Bruker AXS Inc., Madison, WI, 1998.

(19) SAINT, Bruker AXS Inc., Madison, WI, 2000.

(20) Sheldrick, G. M. SHELXTL, Bruker AXS Inc., Madison, WI, 2000.

(21) Wernsdorfer, W. *Adv. Chem. Phys.* **2001**, *118*, 99–190.



**Table 1.** Selected Bond Lengths (Å) and Angles (deg) for Complexes 1–5

	1	2	3	4	5
Mn–O( $\mu_3$ -O <sup>2-</sup> )	1.795–2.129	1.829–1.953	1.775–2.122		
Mn–O( $\mu_2$ -OH)	1.907–2.132				
Mn–O( $\mu_3$ -O <sup>-</sup> )	1.898–2.335	1.919–2.309	1.907–2.338	1.949–2.425	1.937–2.408
Mn–O( $\mu_2$ -O <sup>-</sup> )	1.890–2.161	1.863–2.215	1.889–2.180	1.879–2.127	1.916–2.154
Mn–O(RCO <sub>2</sub> )	1.946–2.176	1.917–2.177	1.993–2.153	1.982–2.153	2.084–2.194
Mn- $\mu_2$ O(RCO <sub>2</sub> )				2.112–2.348	2.189–2.362
Mn- $\mu_2$ O(H <sub>2</sub> tea)					1.886–2.206
Mn–O(H <sub>2</sub> tea)					2.209–2.248
Mn–N	2.059–2.072	2.043	2.059–2.081	2.229	
Mn1 (cis)	82.4–96.2	85.0–100.2	81.5–100.9	81.53–100.47	80.29–100.06
Mn1 (trans)	168.8–177.2	170.1–172.5	165.5–175.0	169.22–171.08	168.35–172.89
Mn2 (cis)	76.0–97.6	73.0–102.1	70.2–103.4	69.44–109.87	71.94–129.42
Mn2 (trans)	163.6–172.3	162.2–171.1	155.7–172.4	155.18–167.31	146.96–164.16
Mn3(cis)	72.4–107.2	79.8–99.5	79.6–95.5	56.89–118.25	74.24–106.47
Mn3(trans)	157.8–165.9	169.6–175.4	169.7–173.0	137.98–174.70	160.02–165.50
Mn4(cis)	84.1–102.3	82.3–106.0	83.2–101.3		
Mn4(trans)	169.9–170.3	166.9–170.8	170.6–173.2		
Mn5(cis)	82.1–101.3		71.6–103.1		
Mn5(trans)	169.6–170.5		154.0–162.9		
Mn6(cis)	73.0–105.2		76.2–96.4		
Mn6(trans)	169.5–175.4		167.0–172.7		
Mn7(cis)	73.1–103.2		84.6–98.0		
Mn7(trans)	172.9–175.4		169.6–175.0		
Mn8(cis)	81.1–103.0				
Mn8(trans)	168.2–170.6				
Mn9(cis)	84.5–102.0				
Mn9(trans)	170.8–171.5				
Mn10(cis)	71.5–113.4				
Mn10(trans)	153.1–161.6				
Mn11(cis)	75.3–98.8				
Mn11(trans)	161.6–174.9				
Mn12(cis)	83.6–95.8				
Mn12(trans)	170.1–178.8				

Å) and also between the methyl arms of adjacent tripod ligands (C...C, ~4.0–4.3 Å).

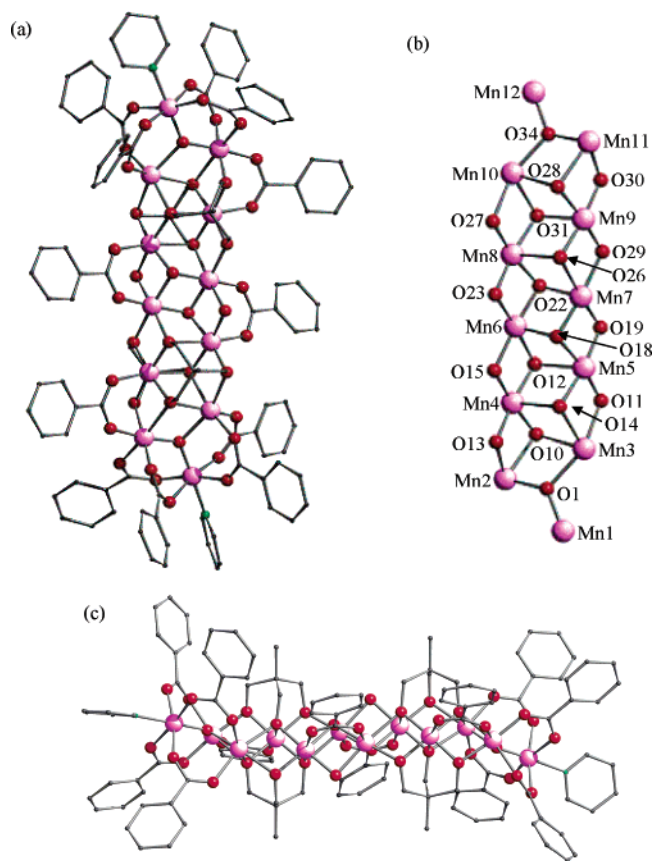


**Figure 1.** (a) Structure of complex 1 viewed from above the central plane of the molecule; (b) The metal–oxygen core of 1; and (c) the structure of 1 viewed from the side of the central plane of the molecule.

The structure of complex 2, [Mn<sub>8</sub>O<sub>4</sub>((CH<sub>3</sub>)<sub>3</sub>CCO<sub>2</sub>)<sub>10</sub>(thme-py)<sub>2</sub>], is shown in Figure 2 and selected bond lengths and angles in Table 1. The core of 2 consists of a [Mn<sup>III</sup><sub>8</sub>O<sub>4</sub>]<sup>16+</sup> rod- or ladder-like unit with Mn1 and Mn8 above and below the plane of the central six Mn ions (Mn2, Mn3, and Mn4, and symmetry

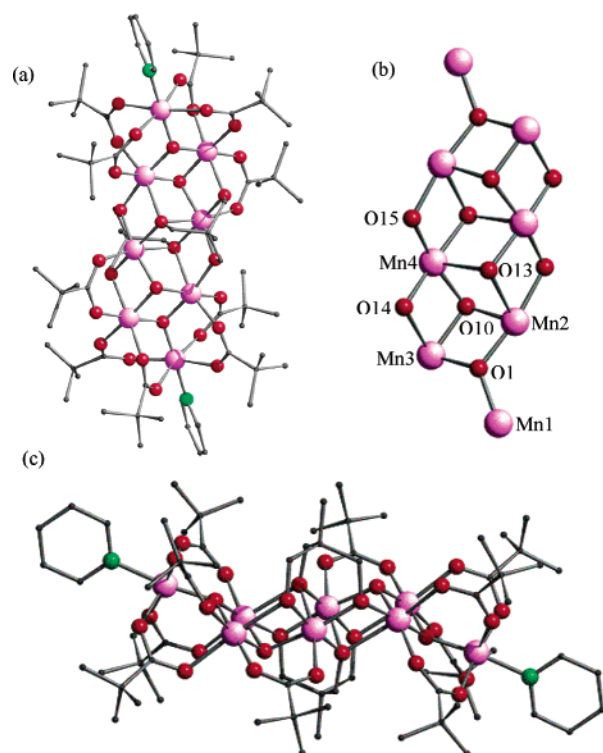


**Figure 2.** (a) Structure of complex 2 viewed from above central plane of the molecule; (b) The metal–oxygen core of 2; and (c) the structure of 2 viewed from the side of the central plane of the molecule.

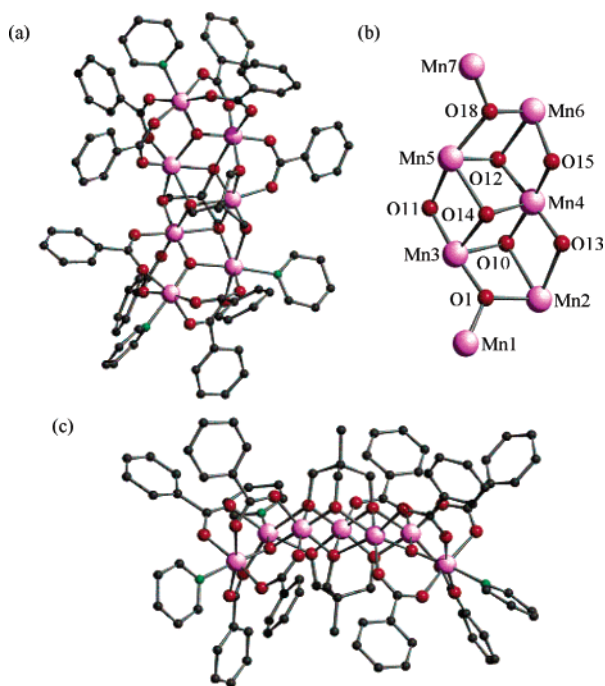


**Figure 3.** (a) Structure of complex **3** viewed from above central plane of the molecule; (b) The metal–oxygen core of **3**; and (c) the structure of **3** viewed from the side of the central plane of the molecule.

equivalents). In this case the core can be described as six edge-sharing triangles or three edge-sharing butterfly units. All eight  $\text{Mn}^{3+}$  ions are in distorted octahedral geometries and display the Jahn–Teller elongations expected for high spin  $\text{Mn}^{3+}$  ions. Again, however, these are not all co-parallel. The two  $\text{thme}^{3-}$  ligands are fully deprotonated and sit above and below the plane of the central six  $\text{Mn}^{3+}$  ions, each using two arms in a  $\mu_2$ -fashion and one arm in a  $\mu_3$ -fashion. The  $(\text{CH}_3)_3\text{CCO}_2^-$  ligands bridge in their usual syn, syn,  $\mu$ -fashion with the two pyridines again providing the capping for the terminal sites on Mn1 and Mn1A. The four  $\text{O}^{2-}$  ions (O1, O10, and symmetry equivalents) are located in the peripheral  $[\text{Mn}_4\text{O}_2]$  butterfly units. There are extensive intermolecular interactions in the crystal of **2**. Each  $[\text{Mn}_8]$  rod sits directly on top of another, creating a column of  $[\text{Mn}_8]$  molecules, with the closest contacts in this direction being between the arms of the tripodal ligands (C...C,  $\sim 3.5$  Å). Between these stacks, the closest contacts are between the methyl groups of the pivalate ions on adjacent molecules (C...C,  $\sim 4.0$  Å), and between the MeCN solvent molecules and the tripod ( $\sim 4.0$  Å) and carboxylate ( $\sim 4.3$  Å) ions.

The structure of complex **3**  $[\text{Mn}_7\text{O}_2(\text{PhCO}_2)_9(\text{thme})_2(\text{py})_3]$  is shown in Figure 3, and selected bond lengths and angles in Table 1. The core of **3** contains a  $[\text{Mn}^{\text{III}}_5\text{Mn}^{\text{II}}_2\text{O}_2]^{15+}$  rod- or ladder-like unit consisting of five edge-sharing triangles, with Mn2 and Mn5 being the  $\text{Mn}^{2+}$  ions. Here, however, both peripheral Mn ions (Mn1, Mn7) are located on the same side of the central five Mn ions. All seven Mn ions are in distorted octahedral geometries, with the five  $\text{Mn}^{3+}$  ions (Mn1, Mn3, Mn4, Mn6, Mn7) displaying nonparallel Jahn–Teller elongations. The two tripodal ligands are fully deprotonated,  $\text{thme}^{3-}$ , and sit above and below the plane of the central five Mn ions, but bridge differently: one uses two arms in a  $\mu_3$ -fashion and one arm in a  $\mu_2$ -fashion, while the second uses two arms in a  $\mu_2$ -fashion and one in a  $\mu_3$ -fashion. The coordination of the Mn ions is again completed by a combination of carboxylate ions and

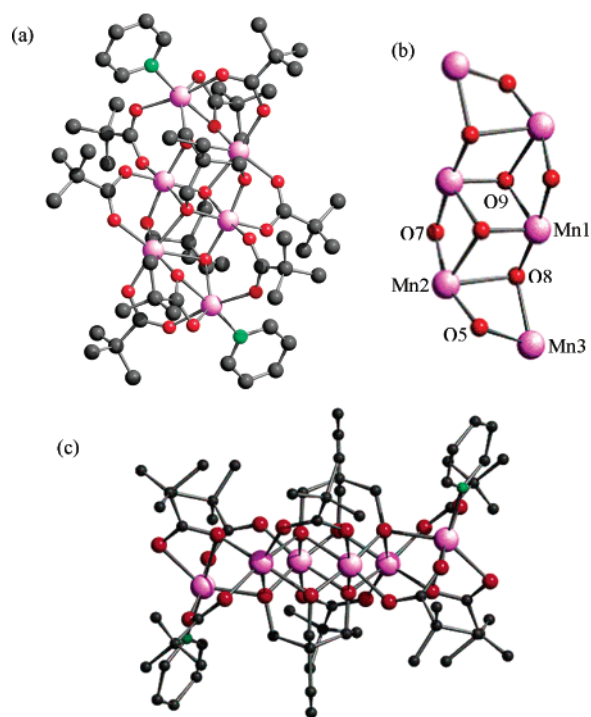


**Figure 4.** (a) Structure of complex **4** viewed from above central plane of the molecule; (b) The metal–oxygen core of **4**; and (c) the structure of **4** viewed from the side of the central plane of the molecule.

pyridine molecules, but in this case in a more asymmetrical manner. There are now three pyridine molecules present: two capping two Mn ions (Mn1, Mn2) at one end of the molecule and one capping Mn7 at the opposite end. The nine  $\text{PhCO}_2^-$  ligands all bridge in their usual syn, syn,  $\mu$ -fashion, but five are located in the ‘half’ of the molecule containing only one pyridine, and the remaining four in the ‘half’ containing the two capping pyridine molecules. The two  $\text{O}^{2-}$  ions are again located in the peripheral  $[\text{Mn}_3\text{O}]$  triangular units. There are also extensive intermolecular interactions in the crystal structure of **3**. This includes  $\pi$ – $\pi$  stacking of the phenyl rings of the benzoate groups on neighboring molecules which effectively forms dimers of  $[\text{Mn}_7]$  units; close contacts between carboxylates and terminal pyridine molecules (C...C,  $\sim 3.8$  Å); and substantial interactions between the MeCN solvent molecules and the terminal pyridines ( $\sim 3.8$  Å), the arms of the tripodal ligands ( $\sim 3.7$ – $4.0$  Å) and the carboxylate ions ( $\sim 3.4$ – $3.8$  Å).

The structure of complex **4**,  $[\text{Mn}_6((\text{CH}_3)_3\text{CCO}_2)_8(\text{tmp})_2(\text{py})_2]$ , is shown in Figure 4 and selected bond lengths and angles given in Table 1. The core of **4** contains a  $[\text{Mn}^{\text{III}}_2\text{Mn}^{\text{II}}_4]^{14+}$  rod- or ladder-like unit consisting of four edge-sharing triangles, with Mn3 and Mn3A above and below the plane of the central four Mn ions (Mn1, Mn2, and symmetry equivalents), with the central two Mn ions (Mn1 and Mn1A) being the  $\text{Mn}^{3+}$  ions. All six Mn ions are in distorted octahedral geometries, with the two  $\text{Mn}^{3+}$  ions displaying the expected Jahn–Teller elongations. In this case, these are co-parallel—approximately perpendicular to the plane of the central four Mn ions. The two tripodal ligands are triply deprotonated,  $\text{tmp}^{3-}$ , and sit above and below the plane of the central Mn ions, each using two arms in a  $\mu_3$ -fashion and one arm in a  $\mu_2$ -fashion. The carboxylates bridge between the metal centers in two different ways: six bridge in their familiar syn, syn,  $\mu$ -mode with each oxygen bonded to one metal ion, while the remaining two bridge in a  $\mu, \eta^1, \eta^2$ -

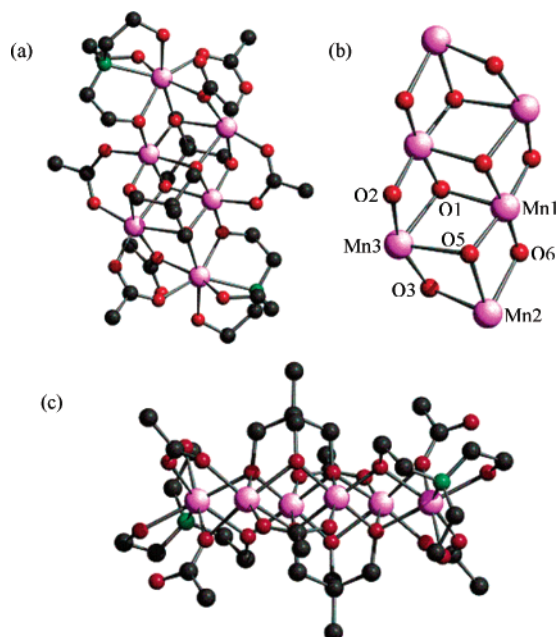


**Figure 5.** (a) The structure of complex **5** viewed from above central plane of the molecule; (b) The metal–oxygen core of **5**; (c) and the structure of **5** viewed from the side of the central plane of the molecule.

mode: using one oxygen to bond to one metal (Mn3) and the second oxygen atom to bridge between the two  $\text{Mn}^{2+}$  ions (Mn2, Mn3) in the peripheral  $[\text{Mn}^{\text{III}}\text{Mn}^{\text{II}}_2]$  triangle. In the crystal the molecules stack directly one on top of the other forming columns in one dimension, with the pivalates on neighboring molecules, approximately 2.7 Å apart (C–H...H–C). Between the columns, the H atoms on the terminal pyridine molecules form close contacts (C–H...O–C, ~2.4 Å) with the oxygen atoms of the carboxylates on neighboring molecules.

The structure of complex **5**,  $[\text{Mn}_6(\text{CH}_3\text{CO}_2)_6(\text{tmp})_2(\text{H}_2\text{tea})_2]$ , is shown in Figure 5 and selected bond lengths and angles given in Table 1. The core of **5** contains a  $[\text{Mn}^{\text{III}}_2\text{Mn}^{\text{II}}_4]^{14+}$  rod- or ladder-like unit consisting of four edge-sharing triangles. This time all six Mn ions effectively lie on the same plane, with the central two Mn ions (Mn1 and Mn1A) being the  $\text{Mn}^{3+}$  ions. All six Mn ions are in distorted octahedral geometries, with the two  $\text{Mn}^{3+}$  ions displaying the expected Jahn–Teller elongations. Again, these are co-parallel—approximately perpendicular to the plane of the central Mn ions. The two tripodal ligands are triply deprotonated,  $\text{thme}^{3-}$ , and sit above and below the plane of the central Mn ions, each using two arms in a  $\mu_3$ -fashion and one arm in a  $\mu_2$ -fashion. The six carboxylates bridge in two different ways: four bridge in the usual syn, syn,  $\mu$ -mode, with the remaining two using only one oxygen atom to bridge between two  $\text{Mn}^{2+}$  ions. The triethanolamine ligands are doubly protonated,  $\text{H}_2\text{tea}^{1-}$ , capping each end of the molecule, using each protonated arm in a terminal fashion, and the deprotonated arm to bridge to the neighboring central  $\text{Mn}^{3+}$  ion. The protonated arms each H-bond to the unbound oxygen of the carboxylate group (2.5 Å) in the same molecule, and in neighboring molecules (2.7 Å). The result is that the molecules pack in sheets in two dimensions, with the sheets separated from each other by a layer of MeCN solvent molecules. In this direction the closest contacts are between the N-atom of the MeCN molecule and the N-atom of the  $\text{H}_2\text{tea}^{1-}$  molecule (4.2 Å).

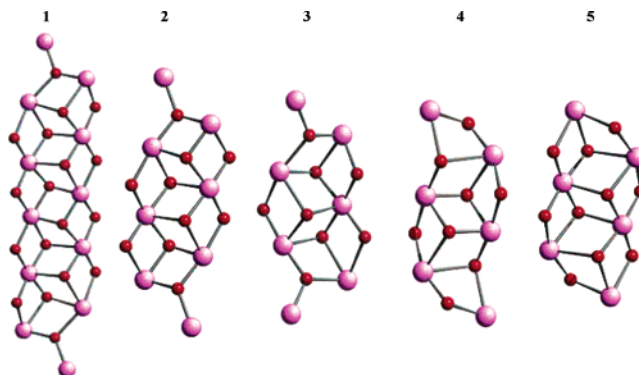


**Figure 6.** Comparison of the metallic cores of complexes **1**, **2**, **3**, **4**, and **5**.

The structures of **4** and **5** are closely related, with the triethanolamine ligands in **5** simply replacing one pyridine and one  $\mu$ ,  $\eta^1$ ,  $\eta^2$  carboxylate in **4**. There are two major differences, however. The first is that in complex **5** all six Mn ions lie in the same plane, while in complex **4** the two peripheral  $\text{Mn}^{2+}$  ions lie above and below the plane of the four central Mn ions. The second is the bridging angles of the  $\mu_3$ -oxygen arm of the tripodal ligand that links the peripheral  $\text{Mn}^{2+}$  ions to the central  $\text{Mn}^{3+}$  ion. For **4**, these angles are 98.68 (Mn1–O–Mn2); 88.73 (Mn2–O–Mn3); and 118.26 (Mn1–O–Mn3), and for complex **5** they are 101.9 (Mn1–O–Mn3); 93.35 (Mn2–O–Mn3); and 101.46 (Mn1–O–Mn2). Thus, the fact that the peripheral ions in **4** are on a different plane to the central ions causes a much larger distortion to the metal–oxygen core. This has important consequences for the observed magnetic behavior (vide infra).

In all cases, the oxidation states of the metal and nonmetal ions were assigned using a combination of charge balance, bond length considerations and BVS calculations.<sup>22</sup>

The structures of complexes **1–5** are clearly closely related (Figure 6). Complex **1** consists of 10 edge-sharing  $[\text{Mn}_3]$  triangles which form a ‘rod’ approximately 17.2 Å in length; complex **2** consists of 6 edge-sharing  $[\text{Mn}_3]$  triangles which form a rod 11.2 Å in length; complex **3** consists of five edge sharing  $[\text{Mn}_3]$  triangles which form a rod 9.2 Å in length; complex **4** consists of 4 edge-sharing  $[\text{Mn}_3]$  triangles which form a rod 8.8 Å in length, and complex **5** consists of 4 edge-sharing  $[\text{Mn}_3]$  triangles which form a rod 8.4 Å in length. In each case the two peripheral Mn ions lie, respectively, above and below the plane described by the remaining central Mn ions, except for complex **3**, where the two peripheral ions lie on the same side of this plane and complex **5** where all six Mn ions effectively lie on the same plane. The topology of this central plane is dictated by the presence of two (**2–5**) or four (**1**) tripodal ligands, which sit directly above and below this plane. In each case (**1–5**), each tripodal ligand bridges five metal centers using all three arms in either a  $\mu_2$  or  $\mu_3$ -fashion. This means that when there are six metals present (**5**) there are no oxides required to bridge between the metal ions. However, when there are seven metals present (**3**, **4**) two oxides are required to bridge between the central five metals and the two peripheral Mn ions, and when eight metals are present (**2**) four oxides are required. Therefore, on going from complex **5** or **4** to complex **3** and then to complex

(22) (a) Brown, I. D.; Altermatt, D. *Acta Crystallogr. Sect. B* **1985**, *41*, 244–247. (b) Zhang, X. Y.; O’Connor, C. J.; Jameson, G. B.; Pope, M. T. *Inorg. Chem.* **1996**, *35*, 30–34. (c) Thorp, H. H. *Inorg. Chem.* **1993**, *32*, 4102–4105.



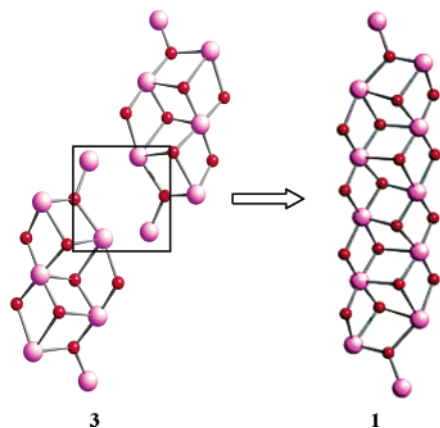


Figure 7. Comparison of the structures of complexes **3** and **1**.

**2** we are essentially just adding one mononuclear  $\{\text{MnO}_2\text{-(RCO}_2)\}$  fragment at a time, to the end of a central core of six Mn ions whose shape (four edge-sharing triangles) is directed by the two tripodal ligands. The increase in the number of oxides present is accompanied by a decrease in the bridging capacity of the tripodal ligands. Even though each remains a  $\mu_5$ -bridge, the number of Mn ions bridged by each individual alkoxide arm decreases: the two tripodal ligands in complex **5** each display a  $\eta^3, \eta^3, \eta^2$ -mode; one of the tripodal ligands in complexes **4** and **3** also displays a  $\eta^3, \eta^3, \eta^2$ -mode, but the second ligand displays a  $\eta^3, \eta^2, \eta^2$ -mode; while both tripodal ligands in complex **2** display a  $\eta^3, \eta^2, \eta^2$ -mode. The change in structure on going from the octanuclear species (**2**) to the dodecanuclear species (**1**) appears, at first, much more pronounced than that observed between complexes **3–5**. However, on closer inspection, the structure of complex **1** can be regarded more simply as two ‘fused’  $[\text{Mn}_7]$  rods (Figure 7). The bonding of the tripodal ligands is identical in the two complexes (two in a  $\eta^3, \eta^3, \eta^2$ -mode; two in a  $\eta^3, \eta^2, \eta^2$ -mode), as are the positions of the  $\text{Mn}^{2+}$  ions.

In trying to understand how complexes **1–5** form, we can perhaps assume that the basic building block consists of a  $[\text{Mn}_6]$  unit comprising four edge-sharing  $[\text{Mn}_3]$  triangles, as directed by the presence of two tripodal ligands. Further cluster growth can then be achieved by one of two methods. The simple addition of mononuclear Mn ions or fragments to each end of the rod, accompanied by the structural rearrangement of carboxylate ions and pyridine molecules that cap each end

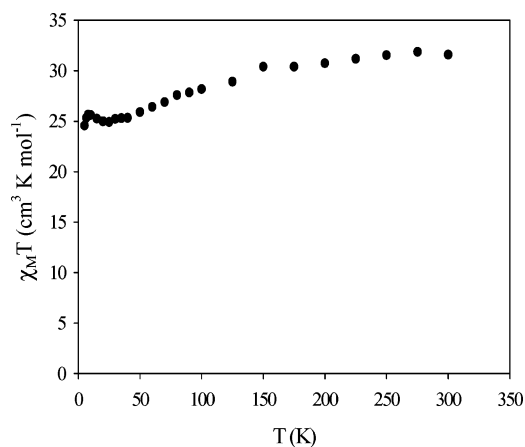


Figure 8. Magnetic susceptibility data for **1**, plotted as  $\chi_{\text{M}}T$  vs  $T$ .

(although this work suggests that perhaps only two more Mn ions can be added before further tripodal ligands are required to stabilize the cluster). Alternatively these  $[\text{Mn}_6]$ ,  $[\text{Mn}_7]$ , or  $[\text{Mn}_8]$  rods can themselves combine in an end-to-end fashion to form much larger oligomers, such as the  $[\text{Mn}_{12}]$  complex, **1**. These rodlike complexes generally only form when the carboxylate used is quite bulky (i.e., benzoate and pivalate). When acetate is used, rodlike structures are not isolated, unless an additional capping ligand (triethanolamine, in this case) is used. This perhaps suggests that rodlike clusters containing acetate are very soluble and that only complexes that exhibit a greater degree of intermolecular interactions are crystallized.

**Magnetic Properties.** Variable temperature dc magnetic susceptibility ( $\chi_{\text{M}}$ ) data were collected on powdered microcrystalline samples of complexes **1–5** in the 1.8–300 K temperature range and in a 5.0 kG (0.5 T) magnetic field. For complex **1** (Figure 8), the  $\chi_{\text{M}}T$  value of approximately  $32 \text{ cm}^3 \text{ K mol}^{-1}$  at 300 K is below that expected for the spin-only value for a  $[\text{Mn}^{\text{III}}_{10}\text{Mn}^{\text{II}}_2]$  unit ( $\sim 39 \text{ cm}^3 \text{ K mol}^{-1}$ ). The value of  $\chi_{\text{M}}T$  remains constant as the temperature is decreased until ca. 150 K when it begins decrease to a value of  $25 \text{ cm}^3 \text{ K mol}^{-1}$  at 1.8 K. This behavior is consistent with the presence of dominant antiferromagnetic interactions between the metal centers with the low-temperature value of  $\chi_{\text{M}}T$  indicating that the molecule has a reasonably large spin ground state. To determine the ground-state spin, magnetization data were collected in the ranges 1.8–10 K and 0.10–2.0 T (Figure 9). The data were fitted by a matrix-diagonalization method to a model that assumes only the ground state is populated, includes axial zero-field splitting ( $D\hat{S}_z^2$ ), and carries out a full powder average.<sup>23</sup> The corresponding Hamiltonian is given by

$$\hat{H} = D\hat{S}_z^2 + g\mu_{\text{B}}\mu_0\hat{S}_zH_z \quad (1)$$

where  $D$  is the axial anisotropy,  $\mu_{\text{B}}$  is the Bohr magneton,  $\mu_0$  is the vacuum permeability,  $\hat{S}_z$  is the easy-axis spin operator, and  $H_z$  is the applied field. The best fit gave  $S = 7$ ,  $g = 1.98$  and  $D = -0.13 \text{ K}$ . When fields up to 7 T were employed the best fit gave  $S = 10$ ,  $g = 1.78$  and  $D = -0.30 \text{ K}$ , but this was of poorer quality than the low field data. This behavior is characteristic of low-lying excited states with  $S$  values greater than the ground state of  $S = 7$ . Low-lying excited states are a common problem when  $\text{Mn}^{2+}$  ions are present since they exhibit weak exchange coupling. The use of only low-field data in the fits can avoid this problem and provide more reliable results.

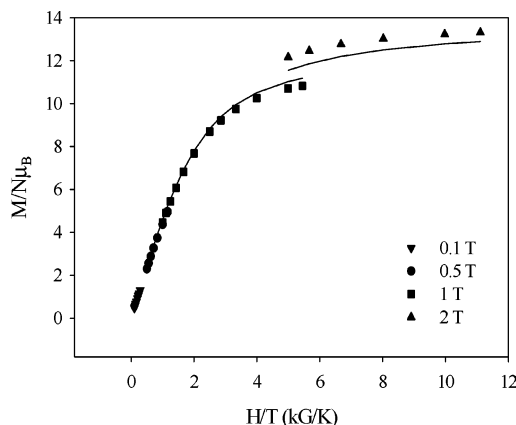
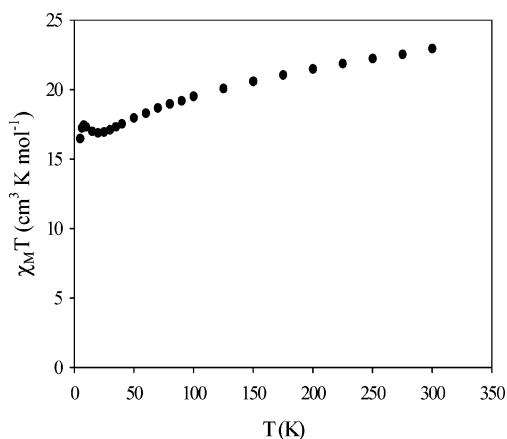


Figure 9. Magnetization data for **1**, plotted as reduced magnetization ( $M/N\mu_{\text{B}}$ ) vs  $H/T$ .



**Figure 10.** Magnetic susceptibility data for **2**, plotted as  $\chi_M T$  vs  $T$ .

For complex **2**, the  $\chi_M T$  value at 300 K, of approximately  $24 \text{ cm}^3 \text{ K mol}^{-1}$  (Figure 10) is consistent with the spin only value expected for a  $[\text{Mn}^{\text{III}}_8]$  unit ( $\sim 24 \text{ cm}^3 \text{ K mol}^{-1}$ ). The value then drops slowly as the temperature is decreased until ca. 20 K where it then increases to a value of  $18 \text{ cm}^3 \text{ K mol}^{-1}$  at 1.8 K. Again, this suggests dominant antiferromagnetic interactions, with the low temperature value indicating that the molecule has a reasonably large spin ground state. Magnetization data (Figure 11) collected in the ranges 1.8–10 K and 0.10–4.0 T gave a best fit of  $S = 6$ ,  $g = 1.81$  and  $D = -0.36 \text{ K}$ .

For complex **3**, the  $\chi_M T$  value at 300 K is approximately  $20.5 \text{ cm}^3 \text{ K mol}^{-1}$  (Figure 12), slightly less than the spin only value expected for a  $[\text{Mn}^{\text{III}}_5\text{Mn}^{\text{II}}_2]$  unit ( $\sim 24 \text{ cm}^3 \text{ K mol}^{-1}$ ). The value then drops steadily as the temperature is decreased until ca. 40 K where it reaches a minimum of  $14.6 \text{ cm}^3 \text{ K mol}^{-1}$ , before increasing to a value of  $21.5 \text{ cm}^3 \text{ K mol}^{-1}$  at 1.8 K, before again dropping to a value of  $20.2 \text{ cm}^3 \text{ K mol}^{-1}$  at 1.8 K. This behavior is indicative of the coexistence of antiferromagnetic and ferromagnetic exchange interactions between the metal ions, leading to the stabilization of a spin ground state with an intermediate value. Magnetization data (Figure 13) collected in the ranges 1.8–10 K and 0.10–4.0 T gave a best fit of  $S = 7$ ,  $g = 1.78$  and  $D = -0.20 \text{ K}$ .

For complex **4** (Figure 14), the room temperature  $\chi_M T$  value of  $22.9 \text{ cm}^3 \text{ K mol}^{-1}$  is slightly lower than that expected for the spin-only value for a  $[\text{Mn}^{\text{III}}_2\text{Mn}^{\text{II}}_4]$  unit ( $23.5 \text{ cm}^3 \text{ K mol}^{-1}$ ). The value of  $\chi_M T$  then drops steadily to  $17.6 \text{ cm}^3 \text{ K mol}^{-1}$  at 70 K, before decreasing more sharply to  $4.8 \text{ cm}^3 \text{ K mol}^{-1}$  at 5.0 K. This indicates dominant antiferromagnetic interactions between the metal centers with a relatively small spin ground state. Magnetization data (Figure 15) collected in the ranges 1.8–10 K and 0.10–3.0 T gave a best fit of  $S = 3$ ,  $g = 1.73$  and  $D = -0.75 \text{ K}$ . However, this fit was of poorer quality than that normally obtained. This is likely due to the presence of multiple  $\text{Mn}^{2+}$  ions and therefore the presence of low-lying excited states. Thus, in this case, the spin ground state cannot be categorically assigned solely on the basis of the dc data, as it is likely that all spin states from  $S = 0$  to  $S = 4$  are very close in energy.

For complex **5** (Figure 16), the room temperature  $\chi_M T$  value of  $23.5 \text{ cm}^3 \text{ K mol}^{-1}$  is consistent with that expected for the spin-only value for a  $[\text{Mn}^{\text{III}}_2\text{Mn}^{\text{II}}_4]$  unit ( $23.5 \text{ cm}^3 \text{ K mol}^{-1}$ ). The value of  $\chi_M T$  remains constant as the temperature is dropped

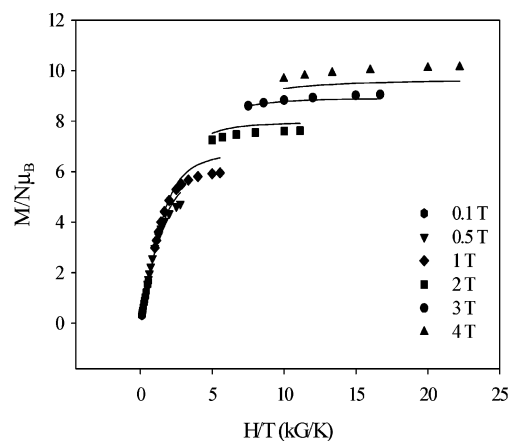


**Figure 11.** Magnetization data for **2**, plotted as reduced magnetization ( $M/N\mu_B$ ) vs  $H/T$ .

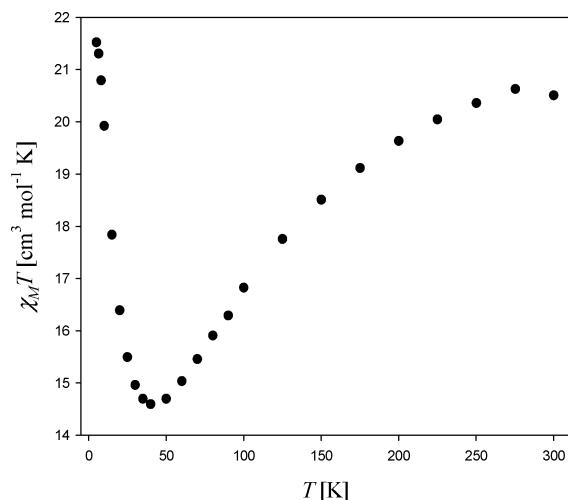


**Figure 12.** Magnetic susceptibility data for **3**, plotted as  $\chi_M T$  vs  $T$ .

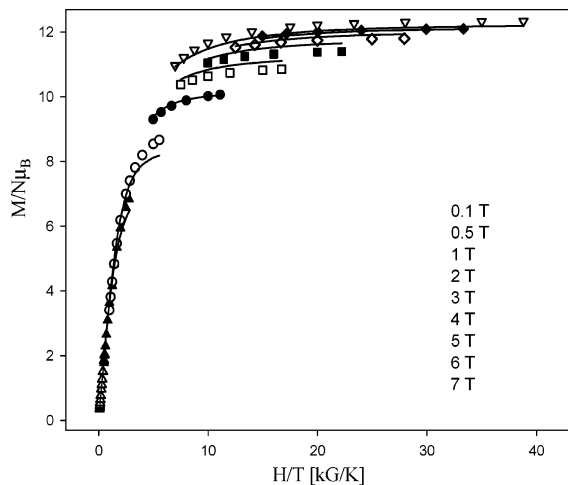


**Figure 13.** Magnetization data for **3**, plotted as reduced magnetization ( $M/N\mu_B$ ) vs  $H/T$ .

until approximately 100 K where the value starts to increase gradually to a maximum of approximately  $25.1 \text{ cm}^3 \text{ K mol}^{-1}$  at 40 K. The value then decreases sharply to a minimum value of approximately  $7.7 \text{ cm}^3 \text{ K mol}^{-1}$  at 1.8 K. As for complex **4**, this behavior is consistent with dominant antiferromagnetic interactions with the low-temperature value of  $\chi_M T$  indicative of a relatively small spin ground state. Magnetization data



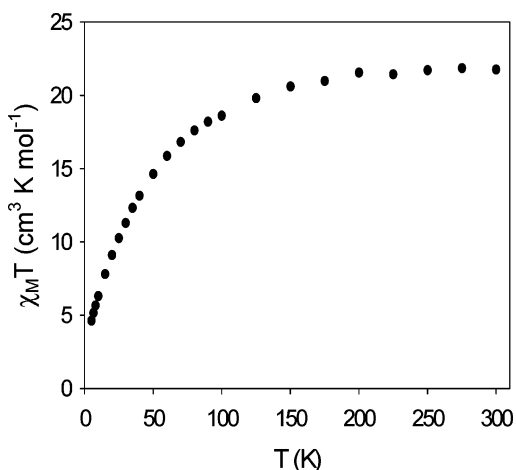


**Figure 14.** Magnetic susceptibility data for **4**, plotted as  $\chi_m T$  vs  $T$ .

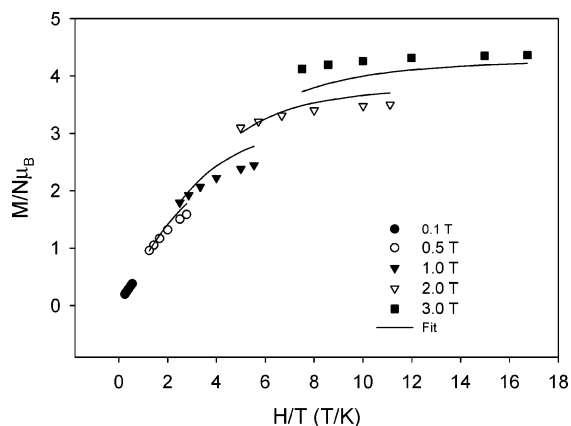


**Figure 15.** Magnetization data for **4**, plotted as reduced magnetization ( $M/N\mu_B$ ) vs  $H/T$ .

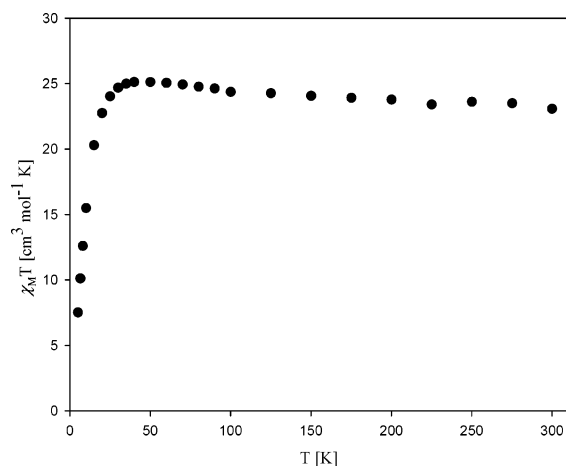


**Figure 16.** Magnetic susceptibility data for **5**, plotted as  $\chi_m T$  vs  $T$ .

collected in the ranges 1.8–10 K and 0.10–3.0 T show an almost linear increase in  $M/N\mu_B$  with increasing field strength. This is probably caused by population of closely lying excited states with higher spin numbers, which become more stable with increasing field. No satisfactory fit of the data was obtained.

The relatively large spin ground states observed for complexes **1–4** presumably arise from the presence of the triangular  $[\text{Mn}_3]$  units, and thus the presence of a number of competing exchange interactions. However, given that all these species are large and complicated molecules, displaying varying degrees of oxidation,

it is impossible to determine the individual pairwise exchange constants  $J_{ij}$  between  $\text{Mn}_i\text{Mn}_j$  pairs through conventional methods. However this problem can be addressed through the use of DFT calculations (vide infra).

**Ac Magnetic Susceptibility Studies.** Given the magnitude of  $S$  and sign of  $D$  obtained for complexes **1–5**, ac magnetization measurements were performed in the 1.8–10 K range in a 3.5 G ac field oscillating at 50–1000 Hz, to check for single-molecule magnetism behavior. However, for all of the above complexes, no peaks were observed in the out-of-phase ac susceptibility measurements. To probe the possibility of SMM behavior at lower temperatures, hysteresis measurements were performed down to 40 mK.

**Single-Crystal Hysteresis Measurements.** Single-crystal hysteresis loop and relaxation measurements were performed using a micro-SQUID setup.<sup>21</sup> Studies of magnetization performed at very low temperature and high fields show that complex **1** behaves as a SMM. Figure 17 presents typical magnetization ( $M$ ) vs applied dc field measurements at a field sweep rate of 0.07 T/s. A hysteresis loop was observed, whose coercivity was strongly temperature and time dependent, increasing with decreasing temperature and increasing field sweep rate, as expected for the superparamagnetic-like behavior of a SMM. The blocking temperature ( $T_B$ ) is  $\sim 1.3$  K. Above this temperature, there is no hysteresis, i.e., the spin relaxes faster to equilibrium than the time scale of the hysteresis loop measurement. The hysteresis loops are not smooth, but show steps at regular intervals of field, indicative of quantum tunneling of the magnetization (QTM). That is, as well as the thermally activated relaxation over the barrier the magnetization is relaxing through the barrier. Relaxation data were determined from dc relaxation decay measurements (Figure 18). First, a large dc field of 1.4 T was applied to the sample at 5 K to saturate the magnetization in one direction, and the temperature lowered to a specific value between 1.5 and 0.04 K. When the temperature was stable the field was swept from 1.4 T to zero at a rate of  $0.14 \text{ T s}^{-1}$  and the magnetization in zero field measured as a function of time. This allows the construction of an Arrhenius plot of  $\ln \tau$  versus  $1/T$  (Figure 19). Above approximately 0.3 K the relaxation rate is temperature-dependent. The straight line in Figure 19 is a fit to the Arrhenius law yielding  $\tau_0 = 1.6 \times 10^{-7} \text{ s}$  and  $U_{\text{eff}} = 18.3 \text{ K}$ . Below ca. 0.3 K however, the relaxation rate is temperature-independent with a relaxation rate of  $3 \times 10^7 \text{ s}$ , indicative of QTM between the lowest energy  $M_s = \pm 7$  levels of the ground state. Single-crystal measurements on complexes **2–5** show no evidence for SMM behavior. This is somewhat surprising given the size of  $S$  and sign of  $D$  seen for **2**, **3**, and **4**. However magnetization vs applied dc field measurements at a field sweep rate of 0.07 T/s indicate of the presence of intermolecular interactions for each species. When these intermolecular interactions are relatively strong, the result is the observation of S-shaped curves with no temperature or sweep rate dependence. This is consistent with the packing of the molecules in the crystal structures of **2**, **3**, and **4** which all show significant inter-cluster interactions. These interactions are likely to be antiferromagnetic, and thus the result is the destruction of any potential SMM behavior that the well-isolated individual clusters may have shown.

**Theoretical Studies.** Although complexes **4** and **5** are structurally very similar, they display quite different magnetic

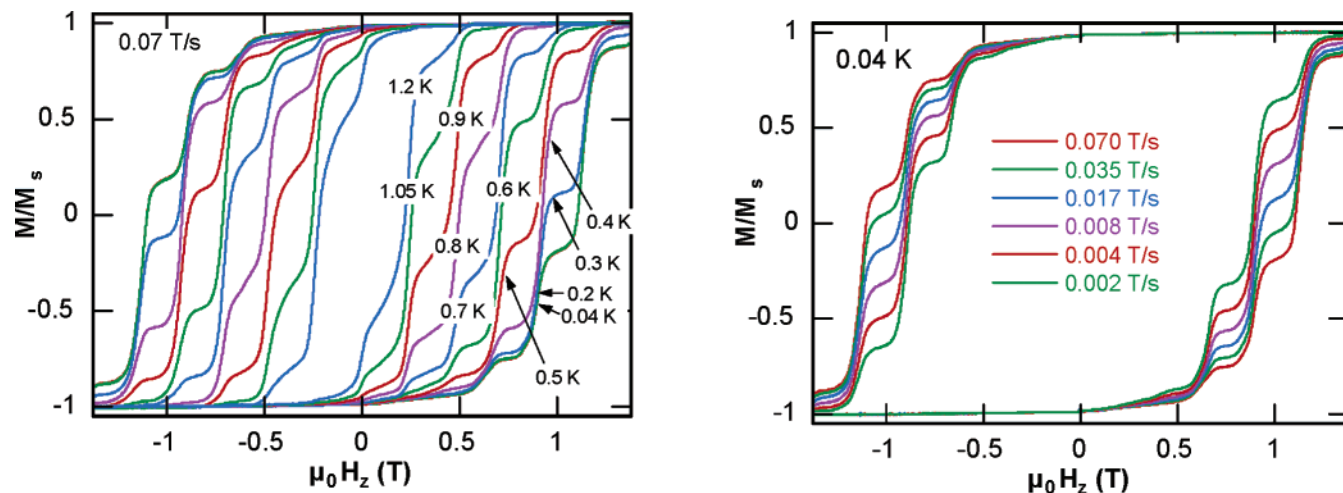


**Figure 17.** Magnetization ( $M$ ) of **1** (plotted as fraction of maximum value  $M_s$ ) vs. applied magnetic field ( $\mu_0 H$ ). The resulting hysteresis loops are shown at different temperatures (left) and different field sweep rates (right).

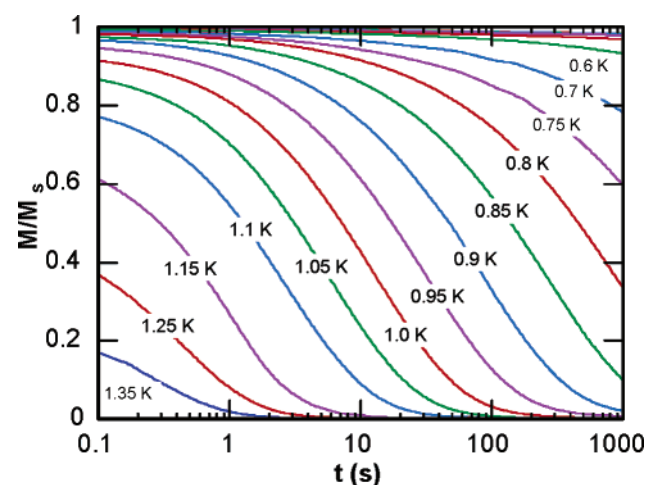


**Figure 18.** Relaxation data for **1**, plotted as fraction of maximum value  $M_s$  vs. time.

behavior. Given our inability to satisfactorily model this behavior and categorically assign spin ground states for both complexes through conventional matrix diagonalization techniques, we have performed DFT calculations to discover both the nature of spin ground states in **4** and **5**, and the magnitudes and signs of the different pairwise exchange interactions present in both. Density functional calculations of the magnetic exchange between paramagnetic metal ions is a new and appealing approach to understanding the magnetic behavior of large, complicated paramagnetic clusters. Noodleman's broken symmetry approach has been widely used to evaluate exchange interactions in metal complexes,<sup>24</sup> and a combination of the B3LYP functional<sup>25</sup> with Ahlrichs basis set<sup>26</sup> has been shown to yield good numerical estimates of exchange interactions.<sup>27</sup> However, these are most commonly employed to calculate the exchange interactions present in dinuclear metal complexes,<sup>28</sup> not for larger clusters. However, Alvarez et al. recently proposed a pairwise interaction model to calculate the exchange interac-

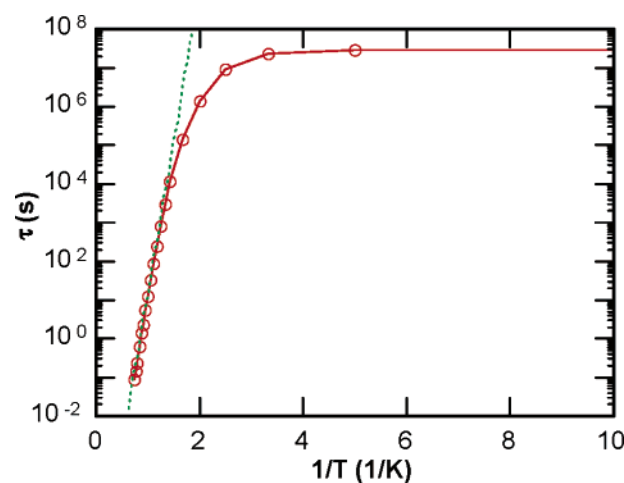


**Figure 19.** Arrhenius plot for **1** using DC decay data on a single crystal. The solid line is the fit of the data in the thermally activated region.

tions in polynuclear transition metal complexes, and this methodology has been shown to give excellent numerical estimates.<sup>28b,29</sup> Therefore, all the calculations in this work use the B3LYP functional with the valence triple- $\zeta$  quality basis sets of Ahlrichs for the metal atoms, and a double- $\zeta$  quality basis set on the nonmetal atoms. All calculations were performed using the program JAGUAR (version 5.0).<sup>30</sup>

The exchange interaction between the metal centers of a binuclear transition metal complex can be calculated using the following expression:

$$J = \frac{(E_{BS} - E_{HS})}{2S_1 S_2 + S_2} \quad (2)$$

where  $E_{BS}$  and  $E_{HS}$  are the energies of the broken symmetry state and high spin state obtained using DFT, respectively, and

(24) Noodleman, L. *J. Chem. Phys.* **1981**, *74*, 5737–5743.  
 (25) Becke, A. D. *J. Chem. Phys.* **1993**, *98*, 5648–5652.  
 (26) (a) Schäfer, A.; Horn, H.; Ahlrichs, R. *J. Chem. Phys.* **1992**, *97*, 2571–2577. (b) Schäfer, A.; Huber, C.; Ahlrichs, R. *J. Chem. Phys.* **1994**, *100*, 5829–5835.  
 (27) Ruiz, E.; Alvarez, S.; Cano, J.; Alemany, P. *J. Comput. Chem.* **1999**, *20*, 1391–1400.

(28) (a) Christian, P.; Rajaraman, G.; Harrison, A.; McDouall, J. J. W.; Raftery, J.; Winpenny, R. E. P. *Dalton Trans.* **2004**, 1511–1512. (b) Abu-Nawwas, A.; Cano, J.; Christian, P.; Mallah, T.; Rajaraman, G.; Teat, S. J.; Winpenny, R. E. P.; Yukawa, Y. *Chem. Comm.* **2004**, 314–315. (c) Ruiz, E.; Alvarez, S.; Rodriguez-Fortea, A.; Alemany, P.; Pouillon, Y.; Massobrio, C. In *Advances in Magnetism: from Molecules to Materials*; Drillon, M., Ed.; Wiley-VCH: Weinheim, **2001**, *7*, 227–279. (d) Rajaraman, G.; Cano, J.; Brechin, K. E.; McInnes, E. J. L. *Chem. Commun.* **2004**, 1476–1477.  
 (29) Ruiz, E.; Cano, J.; Alvarez, S.; Caneschi, A.; Gatteschi, D. *J. Am. Chem. Soc.* **2003**, *125*, 6791–6794.  
 (30) Jaguar 5.0: Schrodinger Inc, Portland, OR, 2003.

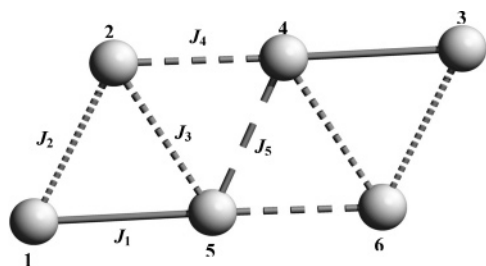


**Figure 20.** Five different exchange interactions that exist between the metal centers in **4** and **5**.

$S_1$  and  $S_2$  are the spins on center 1 and center 2. Calculation of ‘ $n$ ’ different exchange interactions requires the calculation of the energies of ‘ $n+1$ ’ spin configurations. The energy difference between the spin configurations is then related to the exchange interactions using a pairwise interaction model.<sup>29</sup> For both **4** and **5**, there are five chemically different exchange interactions that exist between the metal centers—these are shown in Figure 20. These are classified by taking into account the nature of bridging group between the metal centers and the oxidation state of the metals. The Hamiltonian representing this case, considering only isotropic exchange interactions between neighboring metal centers and ignoring the zero-field splitting terms, is as follows:

$$\hat{H} = -2J_1[\hat{S}_1\hat{S}_5 + \hat{S}_3\hat{S}_4] - 2J_2[\hat{S}_1\hat{S}_2 + J_2\hat{S}_3\hat{S}_6] - 2J_3[\hat{S}_2\hat{S}_5 + \hat{S}_4\hat{S}_6] - 2J_4[\hat{S}_2\hat{S}_4 + \hat{S}_5\hat{S}_6] - 2J_5\hat{S}_4\hat{S}_5 \quad (3)$$

The calculations were performed on model structures of **4** and **5**, replacing the pivalate groups with acetates and the terminal pyridines with ammonia, to reduce the computational cost. The spin configurations chosen to calculate the exchange interactions

in **4** and **5** are shown in Figure 21. The energy differences between the spin configurations has been related to the exchange interactions using a pairwise interaction model and the relationships obtained are as follows:

$$E_{SC1} - E_{SC2} = -25J_1 - 30J_2$$

$$E_{SC1} - E_{SC3} = -25J_1 - 30J_2 - 50J_3 - 20J_4$$

$$E_{SC1} - E_{SC4} = -50J_1 - 50J_3 - 50J_4$$

$$E_{SC1} - E_{SC5} = -30J_2 - 25J_3 - 25J_4$$

$$E_{SC1} - E_{SC6} = -25J_1 - 25J_3 - 25J_4 - 20J_5 \quad (4)$$

The obtained energies of the spin configurations from the DFT calculations for **4** and **5** are shown schematically in Figure 22. The energy ordering of the spin configurations for **4** and **5** differ significantly: the energy scale for **5** is significantly less than that of **4**. This energy difference has been used to obtain the exchange interactions for **4** and **5** using the above equations (4), and the results are summarized in Table 2. All of the interactions are weakly ferromagnetic or weakly antiferromagnetic in nature. This is consistent with the literature values reported for binuclear and polynuclear transition metal complexes containing  $Mn^{2+}$  and  $Mn^{3+}$  ions.<sup>31</sup> The  $J_1$  interactions (between the  $Mn^{3+}$  ( $d^4$ ) and the  $Mn^{2+}$  ions ( $d^5$ )) in **4** and **5** are the strongest interactions of the five, and are antiferromagnetic in **4**, but ferromagnetic in **5**. In **4**, this interaction is mediated through one alkoxide and one carboxylate group. In **5**, however, this interaction is mediated through two alkoxide groups. The orbital counter-complementarity effect associated with dissimilar bridging units could therefore be responsible for the antiferromagnetic interaction in **4**.<sup>32,28a</sup> The  $J_2$  interactions between  $Mn^{2+}$  ions in **4** are mediated through two carboxylate ligands, and

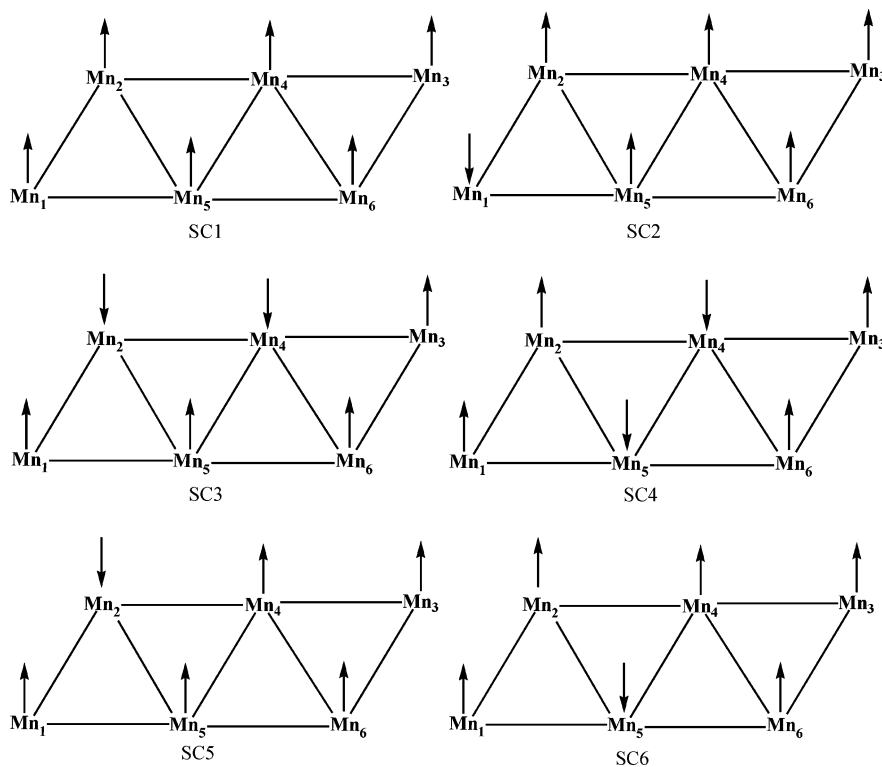


**Figure 21.** Spin configurations chosen to calculate the exchange interactions in **4** and **5**.



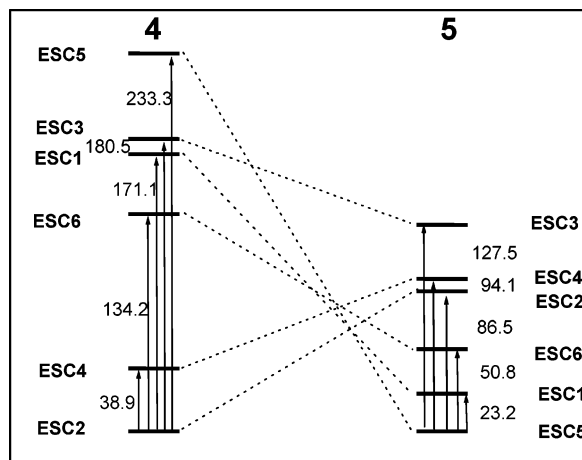


**Figure 22.** Energies ( $\text{cm}^{-1}$ ) of the calculated spin configurations for **4** and **5**, plotted in an energy scale relative to the ground-state spin configuration.

**Table 2.** DFT Computed  $J$  Values for **4** and **5**

exchange ( $\text{cm}^{-1}$ )	<b>4</b>	<b>5</b>
$J_1$	-5.99	+2.44
$J_2$	-0.72	+0.08
$J_3$	+3.02	+0.98
$J_4$	+0.31	-2.00
$J_5$	+1.46	-0.39

therefore are much weaker. In **5**, the  $J_2$  interactions are mediated through one carboxylate and is thus weaker than that observed in **4**. To fit magnetization data for polymetallic complexes, exchange interactions of this kind (i.e. that through carboxylate ligands or three or more atom-bridges) are usually neglected, to avoid over-parametrization. Calculations reveal that this is a valid assumption, as the magnitudes of the exchange interactions are very small. The  $J_3$  interactions ( $\text{Mn}^{2+}-\text{Mn}^{3+}$ ) in **4** and **5** are mediated through an alkoxide bridge and are ferromagnetic in nature. The difference in the magnitude is due to the difference in the  $\text{Mn}-\text{O}-\text{Mn}$  angle. For interactions between  $d^4-d^5$  ions, the interaction becomes less antiferromagnetic or weakly ferromagnetic at larger  $\text{Mn}-\text{O}-\text{Mn}$  angles.<sup>33</sup> In **4**, the  $\text{Mn}-\text{O}-\text{Mn}$  angle is  $106.5^\circ$ , and in **5** the  $\text{Mn}-\text{O}-\text{Mn}$  angle is  $100.1^\circ$ . The  $J_4$  interactions ( $\text{Mn}^{3+}-\text{Mn}^{2+}$ ) in **4** and **5** are mediated through two alkoxide and one carboxylate bridge. This interaction is ferromagnetic in **4**, but antiferromagnetic in **5**. This difference can also be attributed to the difference in the  $\text{Mn}-\text{O}-\text{Mn}$  angles ( $88.5^\circ$ ,  $103.3^\circ$  for **4** and  $95.8^\circ$ ,  $97.9^\circ$  for **5**). The  $J_5$  interactions ( $\text{Mn}^{3+}-\text{Mn}^{3+}$ ) are mediated through two alkoxide groups, and are ferromagnetic in **4**, but antiferromagnetic in **5**. Again, this can be attributed to the small differences in the  $\text{Mn}-\text{O}-\text{Mn}$  angles. Variable temperature magnetic susceptibility data have been calculated for **4** and **5** for the set of exchange interactions given in Table 2, ignoring zero field

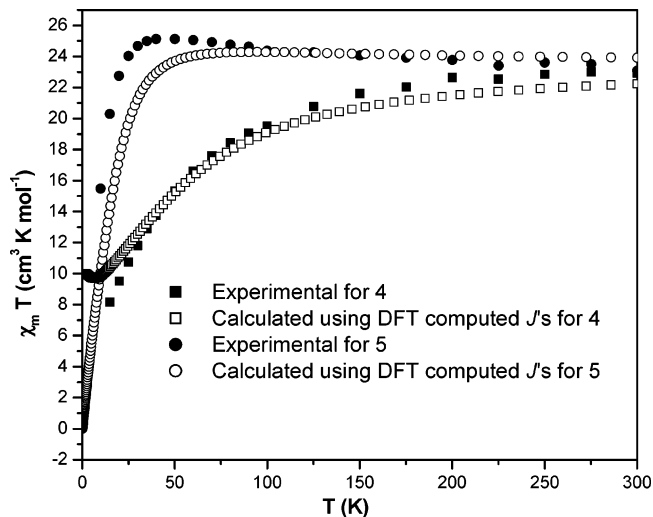


**Figure 23.** Variable temperature magnetic susceptibility data for **4** and **5**. Calculated and experimental values.

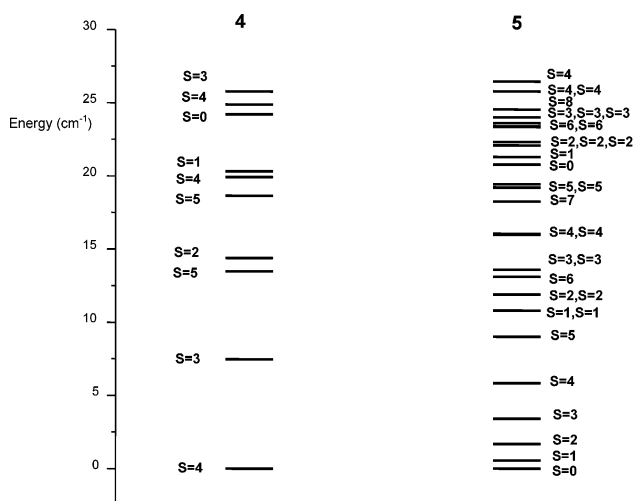


**Figure 24.** Energy spectrum of **4** and **5**, at an energy window  $25 \text{ cm}^{-1}$  from ground state. All energies are relative to the ground state.

splitting (which could be important at low temperatures, given the magnitude of the exchange interactions). The calculated  $\chi_{\text{M}}T$  data at variable temperature has been plotted together with experimental curves in Figure 23. There is very good agreement between the calculated values and experimental results: the calculated values reproduce the shape of the curves in both cases, providing confidence that the sign and magnitude of the exchange interactions are correct, with the deviation at low temperatures due to the absence of the zero-field splitting terms in the Hamiltonian. For **4**, the calculations yield a spin ground state of  $S = 4$ , consistent with experiment, where the magnetization plot suggested a spin ground state of  $S = 3$ . Here, the relatively poor fit to the data was due to the presence of low-lying excited states, with larger  $S$  values. For **5** the DFT calculations suggest a spin ground state of  $S = 0$ —consistent with the experimental evidence. The Eigen values of the energy states obtained for **4** and **5** are plotted in Figure 24, within an energy window of  $25 \text{ cm}^{-1}$  from the ground state. For **4**, the first  $S = 3$  excited-state lies at  $7.5 \text{ cm}^{-1}$ , followed by  $S = 5$  and  $S = 2$  states at  $13.5$  and  $14.4 \text{ cm}^{-1}$ , respectively. For **4**, the first  $S = 1$  excited state lies only  $0.6 \text{ cm}^{-1}$  above the ground state, followed by  $S = 2$  and  $S = 3$  states at  $1.7$  and  $3.4 \text{ cm}^{-1}$ ,

- (31) (a) Yoo, J.; Brechin, E. K.; Yamaguchi, A.; Nakano, M.; Huffman, J. C.; Maniero, A. L.; Brunel, L. C.; Awaga, K.; Ishimoto, H.; Christou, G. *Inorg. Chem.* **2000**, *39*, 3615–3623. (b) Palopli, C.; Sierra, M. G.; Robles, G.; Danhan, F.; Tughagues, J. P.; Signorella, S. *Dalton Trans.* **2002**, 3813–3819. (c) Wittick, L. M.; Murray, K. S.; Moubaraki, B.; Batten, S. R.; Spiccia, L.; Berry, K. J. *Dalton Trans.* **2004**, 1003–1011. (d) Barone, V.; Bencini, A.; Gatteschi, D.; Totti, F. *Chem. Eur. J.* **2002**, *8*, 5019–5027.
- (32) Gutierrez, L.; Alzuet, G.; Real, J. A.; Cano, J.; Borrás, J.; Castiñeiras, A. *Eur. J. Inorg. Chem.* **2002**, *8*, 2094–2102.
- (33) Pilawa, B.; Kelemen, M. T.; Wanka, S.; Geisselmann, A.; Barra, A. L. *Europhys. Lett.* **1998**, *43*, 7–12.

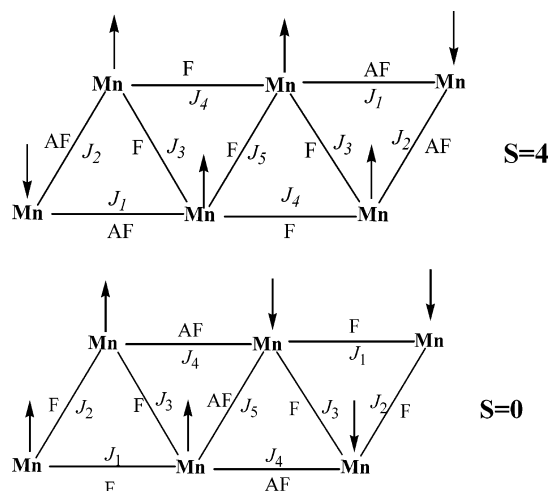


**Figure 25.** Ground-state spin structure of **4** and **5**. F = Ferromagnetic, AF = Antiferromagnetic. ‘Spin-up’ and ‘spin-down’ has been assigned based on the sign of the exchange interactions obtained using DFT.

respectively. In total, there are 31 excited states that lie within  $25\text{ cm}^{-1}$  of the ground state in **5**, and nine excited states within  $25\text{ cm}^{-1}$  of the ground state in **4**. Taking into account the sign of the exchange interactions in **4** and **5**, the ground-state spin structure for each complex can be obtained (Figure 25). For **4**, the ground state of  $S = 4$  results from the central four Mn ions being ‘spin-up’ and the two peripheral Mn ions being ‘spin-down’. For **5**, the  $S = 0$  ground-state results from a ‘spin-up’ alignment on the three Mn ions in one peripheral  $[\text{Mn}_3]$  triangle and a ‘spin-down’ alignment on the other peripheral  $[\text{Mn}_3]$  triangle. In summary, although both clusters have similar metal–oxygen topologies, the nature and magnitude of the exchange interactions differ considerably. The large number of different exchange interactions means that the  $J$ -values cannot be obtained by conventional techniques. Hence, DFT calculations provide a unique method with which to extract the exchange parameters in complicated clusters. These exchange interactions are very important if we are to try to understand differences in the observed magnetic behavior.

## Conclusions

In summary, the use of the tripodal ligands  $\text{H}_3\text{tme}$  (1,1,1-tris(hydroxymethyl)ethane) and  $\text{H}_3\text{tmp}$  (1,1,1-tris(hydroxymethyl)propane) in Mn carboxylate chemistry has produced a family of manganese rodlike complexes whose structures are all derived from a series of edge-sharing triangles. The size of the rod,  $[\text{Mn}_{12}]$  to  $[\text{Mn}_6]$ , is controlled by the identity of both the carboxylate and tripod, and by the presence or absence of base. The formation of clusters containing a series of linked triangular units leads to species with relatively large spin ground states: the largest rod,  $[\text{Mn}_{12}]$ , has a spin ground state of  $S = 7$  and shows single-molecule magnetism behavior; the  $[\text{Mn}_8]$  rod has  $S = 6$ ; the  $[\text{Mn}_7]$  rod has  $S = 7$ . The spin ground state of the  $[\text{Mn}_6]$  rods could not be categorically determined by magnetization measurements. This was due to the presence of multiple  $\text{Mn}^{2+}$  ions in the structure which promote weak exchange interactions and result in the presence of low-lying excited states. Density functional calculations were performed on **4** and **5** in order to establish the ground states for both, and to attempt to understand the differences in the observed magnetic properties. A pairwise interaction model was adopted to obtain the exchange interactions and the calculated results reproduce the shape of the experimental curves. The calculated spin ground states are consistent with experiment and provide an insight into the ground-state spin structure. DFT calculations therefore provide a unique technique for obtaining the exchange interactions present in large and complicated clusters that would otherwise be impossible to determine. Attempts to perform similar DFT calculations on the larger rods are in progress.

**Acknowledgment.** The authors wish to acknowledge Lloyd’s of London Tercentenary Foundation, the EPSRC (United Kingdom), the NSF, and the EPSRC UKCCF for computer time on the Columbus and proton systems.

JA0471929